Asian Journal of Pharmaceutical Sciences 19 (2024) 100967

Available online at www.sciencedirect.com

ScienceDirect

journal homepage: www.elsevier.com/locate/AJPS

Research Article

Alkyl chain length-regulated *in situ* intelligent nano-assemblies with AIE-active photosensitizers for photodynamic cancer therapy

Lingyi Shen[b,1], *Qi-Long Zhang*[b,1], *Yongchao Yao*[d], *Ya-Li Huang*[b], *Zhichang Zheng*[a], *Ming Li*[a], *Hong Xu*[b], *Lin Tan*[a], *Xukun Liao*[a], *Binyi Xia*[a], *Lin Li*[a], *Carl Redshaw*[c], *Yang Bai*[a], *Chengli Yang*[a,e,*]

[a] *Department of Pharmacy, The Affiliated Hospital of Guizhou Medical University, Guiyang 550004, China*
[b] *School of Basic Medicine, Guizhou Medical University, Guiyang 550025, China*
[c] *Chemistry, School of Natural Sciences, University of Hull, Yorkshire HU6 7RX, UK*
[d] *Department of Biotherapy, Cancer Center and State Key Laboratory of Biotherapy, West China Hospital, Sichuan University, Chengdu 610041, China*
[e] *Clinical Research Center, The Affiliated Hospital of Guizhou Medical University, Guiyang 550004, China*

ARTICLE INFO

Article history:
Received 22 December 2023
Revised 8 March 2024
Accepted 3 July 2024
Available online 21 September 2024

Keywords:
Aggregation-induced emission
Photosensitizers
Photodynamic therapy
ROS generation
Self-assembled nanoparticles

ABSTRACT

Photodynamic therapy (PDT) brings new hope for the treatment of breast cancer due to few side effects and highly effective cell killing; however, the low bioavailability of traditional photosensitizers (PSs) and their dependence on oxygen severely limits their application. Aggregation-induced emission (AIE) PSs can dramatically facilitate the photosensitization effect, which can have positive impacts on tumor PDT. To-date, most AIE PSs lack tumor targeting capability and possess poor cell delivery, resulting in their use in large quantities that are harmful to healthy tissues. In this study, a series of AIE PSs based on pyridinium-substituted triphenylamine salts (TTPAs **1–6**) with different alkyl chain lengths are synthesized. Results reveal that TTPAs **1–6** promote the generation of type I and II ROS, including ·OH and $^1O_2$. In particular, the membrane permeability and targeting of TTPAs **4-6** bearing C8-C10 side-chains are higher than TTPAs **1-3** bearing shorter alkyl chains. Additionally, they can assemble with albumin, thereby forming nanoparticles (TTPA **4–6** NPs) *in situ* in blood, which significantly facilitates mitochondrial-targeting and strong ROS generation ability. Moreover, the TTPA **4–6** NPs are pH-responsive, allowing for increased accumulation or endocytosis of the tumor and enhancing the imaging or therapeutic effect. Therefore, the *in vivo* distributions of TTPA **4–6** NPs are visually enriched in tumor sites and exhibited excellent PDT efficacy. This work demonstrates a novel strategy for AIE PDT

* Corresponding author.
E-mail address: yangcl714@163.com (C. Yang).
[1] These authors contributed equally to this work.
Peer review under responsibility of Shenyang Pharmaceutical University.

https://doi.org/10.1016/j.ajps.2024.100967

and has the potential to play an essential role in clinical applications using nano-delivery systems.

1. Introduction

According to statistics, cancer has been the second leading cause of death worldwide over a number of decades [1]. For example, in China, the incidence and mortality of breast cancer ranks first among malignant diseases in women. It accounts for 6.9 % of the mortality of all female malignant tumors [2]. At present, radical mastectomy, commonly used in clinical practice, requires breast resection, which brings great psychological and physiological trauma to women. Moreover, surgical treatment is ineffective for metastatic lesions, and most deaths from breast cancer are caused by metastatic lesions [3]. Therefore, the search for new breast cancer treatments is of great importance.

Compared with traditional surgery, chemotherapy or radiotherapy, photodynamic therapy (PDT) can efficiently kill tumor cells with few side effects and can be temporally and spatially controlled by light [4–7]. Therefore, PDT could bring new hope for the treatment of breast cancer and myocardial ischemia-reperfusion injury [8,9]. Photosensitizers (PSs), which can be envisaged as a type of PDT drug, generate a large amount of highly cytotoxic reactive oxygen species (ROS) upon irradiation with a specific laser and furnish favorable anti-tumor effects. Therefore, the effectiveness of PDT depends on the photocytotoxic reaction caused by the pre-activation of PSs in the body [10–12].

The ROS is mainly divided into type I, including hydroxyl radical (·OH), hydrogen peroxide (H_2O_2) and superoxide ($O_2^{-}\cdot$) and type II, including singlet oxygen ($^1O_2$) [13,14]. Moreover, recent studies have revealed that type I ROS possess higher cytotoxicity compared with type II ROS in addition to producing extra oxygen *in situ*, and thus can dramatically regulate the tumor hypoxia surroundings. However, the majority of recently reported PSs following the type II pathway are confronted with a fundamental paradox between the hypoxic microenvironment of a solid tumor and the serious oxygen-consumption associated with PDT [15–18]. Thus, there is a desperate need to develop photosensitizers with high PDT yet lower O_2-dependence. Consequently, and with a view to achieving excellent tumor diagnosis and therapy effects, the use of organic fluorescent PSs for bioluminescence imaging diagnosis and PDT applications has received much attention. Nevertheless, traditional organic PSs usually lead to conventional fluorophores with weak emission or even being non-emissive and ROS production reduced due to π–π stacking in the aggregation state and/or at high concentration, which is often referred to as aggregation-caused quenching (ACQ) and has an unfavorable influence on PDT clinical application [19–21]. Due to the defects of ACQ, a new type of PSs with aggregation-induced luminescence (AIE) properties has gradually received increased attention in PDT [22–24]. For the AIE-PSs, the non-radiative internal conversion leads to energy attenuation released by the singlet state through radiative transition or cross-channeling between systems by limiting the intramolecular motion in the aggregation state, which is conducive to enhancing the relative intensity of fluorescence and providing sufficient ROS generation, especially in an aerobic/anoxic environment [25–27]. On the other hand, since most photosensitizers usually lack tumor targeting and have poor self-delivery, they can only be used for PDT by intratumoral injection [28,29]. Therefore, changing the side-chain length to improve membrane permeability [30,31] and targeting [32] has gradually become an important method for molecular drug design because of its simplicity and efficiency. Mitochondria, as energy factories in cells, are often used as important targets for anti-tumor research. Moreover, based on the large negative mitochondrial membrane potential (MMP), mitochondria-targeting molecules are usually designed to be cationic, thus achieving targeting based on electrostatic attraction [33]. Additionally, Tangs team has also demonstrated that when the MMP is decreased or vanished, the hydrophobic interactions induced by long alkyl chains can be retained in the mitochondria for a prolonged period [34].In order to improve both permeability and targeting, we have synthesized a series of AIE molecules with different lengths of alkyl chains (named TTPAs **1–6**, the number of carbon atoms in the alkyl chain of the TTPA varies from 5 to 10) and then investigated their physicochemical properties and PDT effects (Scheme 1). All six AIE molecules can generate an assortment of ROS of type I (·OH) and type II ($^1O_2$). Moreover, the results of this work shed light on an interesting phenomenon, namely that lengthening the alkyl chain in the TTPA molecules enhances their capacity to target the mitochondria. Moreover, TTPAs **4–6** can assemble with albumin to form TTPA **4–6** nanoparticles in blood or complete culture medium and provide favorable conditions for their enrichment in tumor sites *in vivo* because here nanostructures have been identified that exhibit significant superiority, including size-dependent physical properties, long cycle times and which can be used for active targeting [35–37]. In addition, these assembled TTPA **4–6** nanoparticles can greatly facilitate tumor targeting and further increase PDT efficiency. Lastly, these AIE molecules can be excited to fluoresce in the near-infrared region (NIR) and, consequently, visualized therapy can be achieved *in vivo*. This study opens new avenues for efficient tumor imaging and for the precise treatment of breast cancer.

2. Materials and methods

2.1. *Materials*

The cell-counting-kit (CCK8, 500 T), 2′,7′-dichlorodihydrofluorescein (DCFH), 2′,7′-dichlorodihydro (DCF) and 2′,7′-

dichlorodihydrofluorescein diacetate (DCFH-DA) were all obtained from Dalian Meilun Biotechnology Co., Ltd. (Dalian, China). The calcein AM/PI staining kits were bought from Biosharp life sciences (Hefei, China). 9,10-Anthracenediyl-bis (methylene) dimalonic acid (ABDA), chlorin e6 (Ce6), hydroxyphenyl fluorescein (HPF), 5,5-dimethyl-1-pyrroline-N-oxide (DMPO) and 2,2,6,6-tetramethylpiperidine (TEMP) were purchased from Sigma-Aldrich (Saint Louis, USA). The green LysoTracker and Mito-Tracker were both obtained from Invitrogen (Carlsbad, USA). The bovine serum albumin (BSA) and RPMI-1640 culture medium were purchased from Gibco BRL (Carlsbad, USA). The fetal bovine serum (FBS) was obtained from Thermo-Fisher (Massachusetts, USA). Dimethyl sulfoxide (DMSO) of analytical grade was obtained from Aladdin (Shanghai, China). The three cell lines, including mouse breast cells (4T1), skin melanoma cells (B16F10) and colon cancer cells (CT26), were provided by the State Key Laboratory of Biotherapy. They were all cultivated in 1640 RPMI medium with 10% FBS.

2.2. *Apparatus and characterization*

NMR spectra were measured using an Inova-600 Bruker AV 600 spectrometer (Bruker, Karlsruhe, Germany) and DMSO–d_6, including tetramethylsilane (TMS) as an internal standard, was used as a solvent. MS-ESI spectra were recorded with Xevo G2-S QTof spectrometer (Waters, USA). Fluorescence spectroscopy measurements were recorded on a Cary Eclipse Hitachi 4500 spectrophotometer (Hitachi, Tokyo, Japan) (Varian). Single-crystal X-ray diffraction was conducted on a Bruker Smart Apex II single-crystal diffractometer (Bruker, Karlsruhe, Germany). The types of ROS produced by TTPAs with light were determined by electron spin resonance (ESR, Bruker EMX PLUS, Germany). Size and Zeta potential of nanoparticles were measured using a NanoBrook 90plus PALS analyzer (Brookhaven Instruments USA). The morphology of the nanoparticles was imaged by a transmission electron microscope (TEM, H7800, Tokyo, Japan). The flow cytometry measurements were recorded on a Flow Cytometer (Beckman Coulter, CA, USA). Confocal fluorescence microscopy was imaged by a ZEISS microscope (ZEISS, LSM 710, Germany). *In vivo* fluorescence imaging was performed by a Bio-real imaging system (IVIS Lumina Series III, Austria).

2.3. *General procedure for preparation of TTPAs 1–6*

Methyl pyridinium bromide salts were prepared as described previously [38]. The synthetic procedure for compounds TTPA **1–6** is shown in Scheme 1. A mixture of compound a (1.2 mmol) and compound b (1.0 mmol) that was prepared according to previous work [39] was added to 60 ml ethanol. Then, a few drops of piperidine as a catalyst was added and the mixture was refluxed overnight. After cooling to room temperature, the solvent was removed *in vacuo* to obtain the crude product. Silica-gel column chromatography was used for further purification with dichloromethane/methanol (8/1, *v*/*v*) as eluent. The chemical structures of the TTPAs **1–6** were confirmed by NMR spectroscopy (Figs. S1–S6) and MS data (Figs. S7–S12).

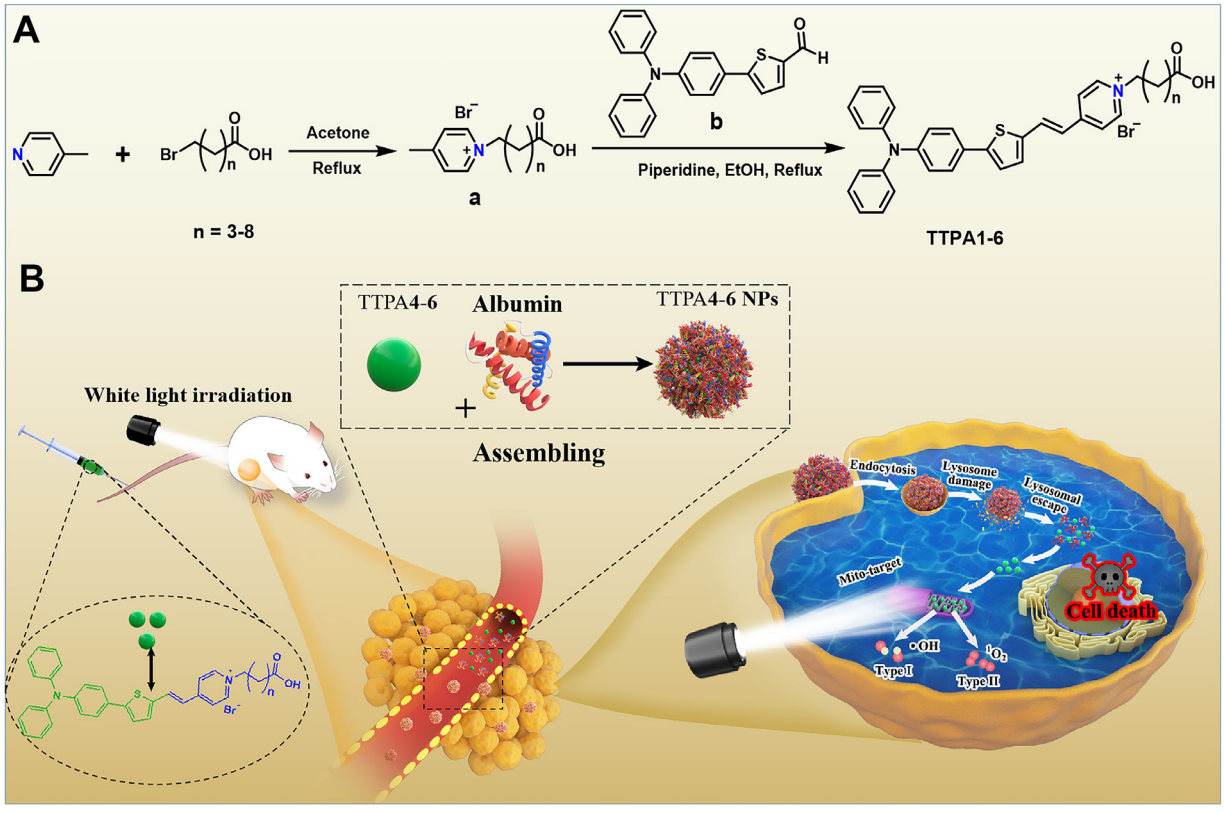

Scheme 1 – (A) Schematic diagram of the synthesis of TTPAs 1–6; (B) Construction of TTPAs 4–6 nanoparticles and their application in photodynamic tumor therapy.

2.4. ROS generation ability assay

DCFH (10 μl, 10 μM) as an indicator was mixed with TTPAs **1–6** (10 μM) or the free Ce6 in PBS solution (1 ml) [40]. After irradiation with white light (50 mW/cm^2) over different time durations, the fluorescence spectra of DCF were measured at 480 nm. DCFH alone was tested under the same experimental conditions as the control group.

2.5. Hydroxyl radical species generation ability test

HPF (5 mM in DMF, 2 μl) as a ·OH tracker was mixed with AIEgens (TTPAs **1–6**, 10 μM) or free Ce6 (10 μM, as active control) of 1× PBS solution (1 ml). The fluorescence spectra of HPF were recorded under 480 nm (excitation wavelength) after irradiation with white light (50 mW/cm^2) over different time durations. The relative emission intensity (I/I_0–1) variation with irradiated time at 512 nm was then plotted. The fluorescence intensity of HPF alone was determined as the control group.

2.6. Detection of $^1O_2$ generation ability test

The singlet oxygen ($^1O_2$) generated by TTPAs **1–6** was measured through a universally used singlet oxygen capture agent named ABDA, and the experiment was conducted in accordance with the protocol previously reported [41]. Briefly, 200 μM ABDA was mixed with 10 μM TTPAs **1–6** in PBS. In addition, free Ce6 (10 μM) and PBS were utilized as the control groups. Consequently, all the TTPAs **1–6** and free Ce6 groups were irradiated with white light (~50 mW/cm^2). Finally, the absorbance change of ABDA under different duration white light-irradiation at 378 nm was recorded by an ultraviolet spectrophotometer.

2.7. ROS detection by ESR analysis

ESR analysis was performed to monitor the generation of ROS types using TEMP as spin-trap agent for $^1O_2$ and DMPO for ·OH. TTPAs (30 μl, 1 mM in PBS with 1 % DMSO) and 30 μl capture agent DMPO or TEMP (50 mM in PBS) were mixed. Spectra of spin was monitored in a range of 3460–3560 G after the solution was irradiated by irradiation with simulated sunlight of 100 W/cm^2 for 5 min. Background interference was corrected using the sample before irradiation.

2.8. Cellular uptake analysis and distribution assay of TTPAs 1–6

To evaluate the uptake rate of TTPAs **1–6**, 4T1 cells were plated on coverslips in a 24-well plate with the amount of 5 × 10^4 cells per well. After 24 h, the original culture medium was discarded and fresh medium containing 10 μl TTPAs **1–6** stock solutions (1 mM in DMSO) was added. After 1 h, the cells were washed with PBS and fixed with paraformaldehyde for about 10 min. Finally, the cells were imaged by confocal microscopy after the cell nuclei were stained with DAPI.

In order to observe the lysosomes distribution of TTPAs **1–6**, 5 × 10^4 4T1 cells were inoculated in a 24-well cell culture plate and incubated with cell culture medium for 24 h. The medium was replaced with a fresh one containing TTPAs **1–6** stock solutions at a final concentration of 5 μM and incubated for 0.5 h, 1 h and 2 h. Then, the cells mitochondria were labeled with green Lysosome-Tracker (50 nM) for 30 min [42]. Next, the cells were fixed with 4 % PFA and nuclei were stained with DAPI. Finally, the mitochondrial targeting of TTPAs **1–6** in the 4T1 cells was imaged by CLSM. The entry of TTPAs **1–6** into mitochondria is the key to its role in PDT. Nevertheless, we have further evaluated the mitochondria targeting assay of the TTPAs **1–6**. 5 × 10^4 4T1 cells were inoculated in a 24-well cell culture plate and incubated with cell culture medium for 24 h. The medium was replaced with a fresh one containing TTPA **1–6** stock solutions at a final concentration of 5 μM and incubated for 2 h. Then, the cells' mitochondria were labeled with green Mito-Tracker (50 nM) for 30 min [43]. Next, the cells were fixed with 4 % PFA and nuclei were stained with DAPI. Finally, the mitochondrial targeting of TTPAs **1–6** in the 4T1 cells was imaged by CLSM.

2.9. 3D tumor penetration of TTPAs 1–6

4T1 cells were seeded into 6-well plates that were pre-coated with 1 ml agarose and cultured for 5 d to form multicellular spheroids. Then, the tumor spheroids were treated with TTPA **1–6** stock solutions at a final concentration of 10 μM. After 2 h, the fluorescent intensity of each group was observed by CLSM.

2.10. Mitochondrial superoxide generation assay

4T1 cells were seeded into cell culture plate containing coverslips. After 24 h, TTPA **1–6** stock solutions at a final concentration of 10 μM were added and incubated for 24 h. Thereafter, the cells were stained with Mito-SOX. Finally, the cells were exposed to white light (~50 mW/cm^2) for 2 min. Finally, the mitochondrial superoxide was detected and imaged by CLSM.

2.11. ROS generation intracellular

Next, the ROS generation during PDT therapy was detected by a ROS-captured molecule named DCFH-DA [44]. 4T1 cells were placed into a 24-well plate containing coverslips at a density of 5 × 10^4 cells and incubated overnight. Then, the old medium was replaced by a culture medium with TTPA **1–6** stock solutions at a concentration of 10 μM and then exposed to white light (~50 mW/cm^2) for 2 min. After 12 h, the original medium was replaced by fresh medium with 10 μM DCFH-DA and incubated for another 20 min at 37 °C. Finally, the nuclei were labeled with DAPI before being observed by CLSM. Furthermore, the cells were also collected, and the fluorescence was detected by a flow cytometer.

2.12. Mitochondrial morphology observation

4T1 cells were treated with PBS or TTPAs **1–6** stock solutions in the complete culture medium at a final concentration of 10 μM for 0.5 h and further radiated with white light (~50 mW/cm^2)

for 2 min. Subsequently, 4T1 cells were harvested and fixed in phosphate-buffered glutaraldehyde. Min later, 4T1 cells were simultaneously dehydrated in cold-graded ethanol. Meanwhile, the 4T1 cells in each group were incubated in Epon 812/acetone (2:1) overnight and then replaced with pure Epon812. Each group of 4T1 cells was further polymerized at 30, 45 and 60 °C for 3 d. The 4T1 cells were photographed using a Hitachi TEM.

2.13. *PDT effect in vitro*

CCK8 assay and a Live-dead cell staining kit were used to evaluate the photodynamic cell killing effect. For the CCK8 assay, 4T1, CT26 and B16F10 were inoculated in a 96-well plate at the amount of 2×10^3. After 24 h, the new culture medium with different final concentrations of TTPAs **1–6** in a complete culture medium (3.125, 6.25, 12.5, 25, 50 and 100 μM) replaced the older one. After 4 h, the plates containing the 4T1 cells were exposed to white light (~50 mW/cm^2) for 5 min, and another group of plates containing 4T1 cells were kept in darkness as a control. For another 48 h, CCK8 was added to each well, and the absorbance was read at 450 nm on a microplate reader. Cell viability was calculated by reference to the control group. To observe the effect of cell killing more directly, a Calcein AM/PI test was carried out after the cells were treated with 10 μM TTPAs **1–6** and subsequently (after 4 h) exposed to white light. Then, the cells were stained in accordance with the manufacturer's instructions before being observed with CLSM.

2.14. *Cytotoxicity assays*

The 4T1 cells were used to evaluate the dark toxicity of the TTPA **1–6** molecules without white light irradiation. In brief, 2×10^3 cells per well of 4T1 were seeded in a 96-well cell culture plate and incubated with complete culture medium for 24 h. Thereafter, the primary medium was replaced by fresh medium containing a certain concentration gradient (3.125, 6.25, 12.5, 25, 50 and 100 μM) of TTPA **1–6** compounds. After 48 h, the UV absorbance was read at 450 nm on a microplate reader after incubating with CCK8. The cell cytotoxicity was calculated using the same method used above.

2.15. *Preparation and characterization of assemblies from TTPAs 1–6*

The particle size and zeta potential of TTPAs **1–6** were measured by dynamic light scattering (DLS) method. In brief, stock solutions of TTPAs **1–6** were respectively prepared with DMSO at a concentration of 1 mM. Subsequently, 10 μl stock solution of each TTPA **1–6** was added into PBS to a final volume of 1 ml. In order to investigate the characterization of TTPAs **1–6** assembled with BSA (a substitute for serum albumin), 10 μl TTPAs **1–6** (1 mM in DMSO) were separately mixed with 10 μl the stock solution of albumin (1 mM in PBS), followed by dilution with the PBS (980 μl). Finally, the particle size and zeta potential of these mixed solutions were measured on a Brookhaven Instrument. In addition, in accordance with the DLS results, the morphology and size distribution of TTPA **4–6** nanoparticles were observed by TEM following negative staining using phosphotungstic acid.

2.16. *Fluorescence intensity measurements TTPAs 4–6*

The fluorescence spectra of each compound TTPA **4–6** (-albumin) and TTPA **4–6** nanoparticles (+albumin) were recorded with a fluorescence spectrometer. Additionally, all the TTPAs **4–6** and TTPA **4–6** nanoparticles possessed a unitive concentration of 10 μM in PBS (with 10 μl DMSO stock solution). Finally, the fluorescence intensity was measured at an excitation wavelength of 498 nm and the emission was collected from 500 to 850 nm.

2.17. *Molecular modeling of interaction of TTPAs 4–6 with albumin*

To estimate the possible interaction of the protein and TTPA molecules further, TTPA 4, TTPA 5, and TTPA 6 were docked with albumin by autodock vina. The structure of albumin was obtained from the RCSB Protein Data Bank (PDB ID: 3V03) and TTPA molecules was modelled by the program of ChemDraw. The predicted assemblies were then optimized and ranked according to Screen Score, an empirical scoring function. Each operation screened 100 conformations for each assembly that were advantageous for docking.

2.18. *Formation of albumin complexes in blood*

The fluorescence spectra of TTPAs **4–6** alone, and mixtures of TTPAs **4–6** with plasma and blood separately were performed. For the TTPAs **4–6** alone experiments, the PBS (phosphate buffered saline) solutions of TTPA **4–6** (10 μM, containing 1 % DMSO) were used. For the experiments with the mixtures, TTPAs **4–6** (each in 10 μl DMSO) were separately mixed with plasma and blood, followed by dilution with the PBS (980 μl) for each sample.

2.19. *Animal models*

The BALB/c mice were purchased from the Beijing HFK Bioscience Co., Ltd (Beijing, China), and all experiments were conducted under protocols approved by The Clinical Medical Research Center SPF Animal Laboratory, an affiliated hospital of Guizhou University. The subcutaneous 4T1 model was generated by injection of 1×10^6 of 4T1 cells in a serum-free medium into each mouse. Then, the tumor volume was calculated by a Vernier caliper.

2.20. *In vivo fluorescence distribution*

In order to observe the *in vivo* distribution of TTPAs **4–6**, the tumor-bearing mice model built above was divided into three groups ($n = 3$). As the tumor volume reached about 300 mm^3, the TTPAs **4–6** were injected through a tail vein. Lastly, the average fluorescence intensity of TTPAs **4–6** was imaged and calculated by an *in vivo* fluorescence imaging system. It is emphasized that the excitation and emission wavelengths are set to 507 nm and 610 nm, respectively.

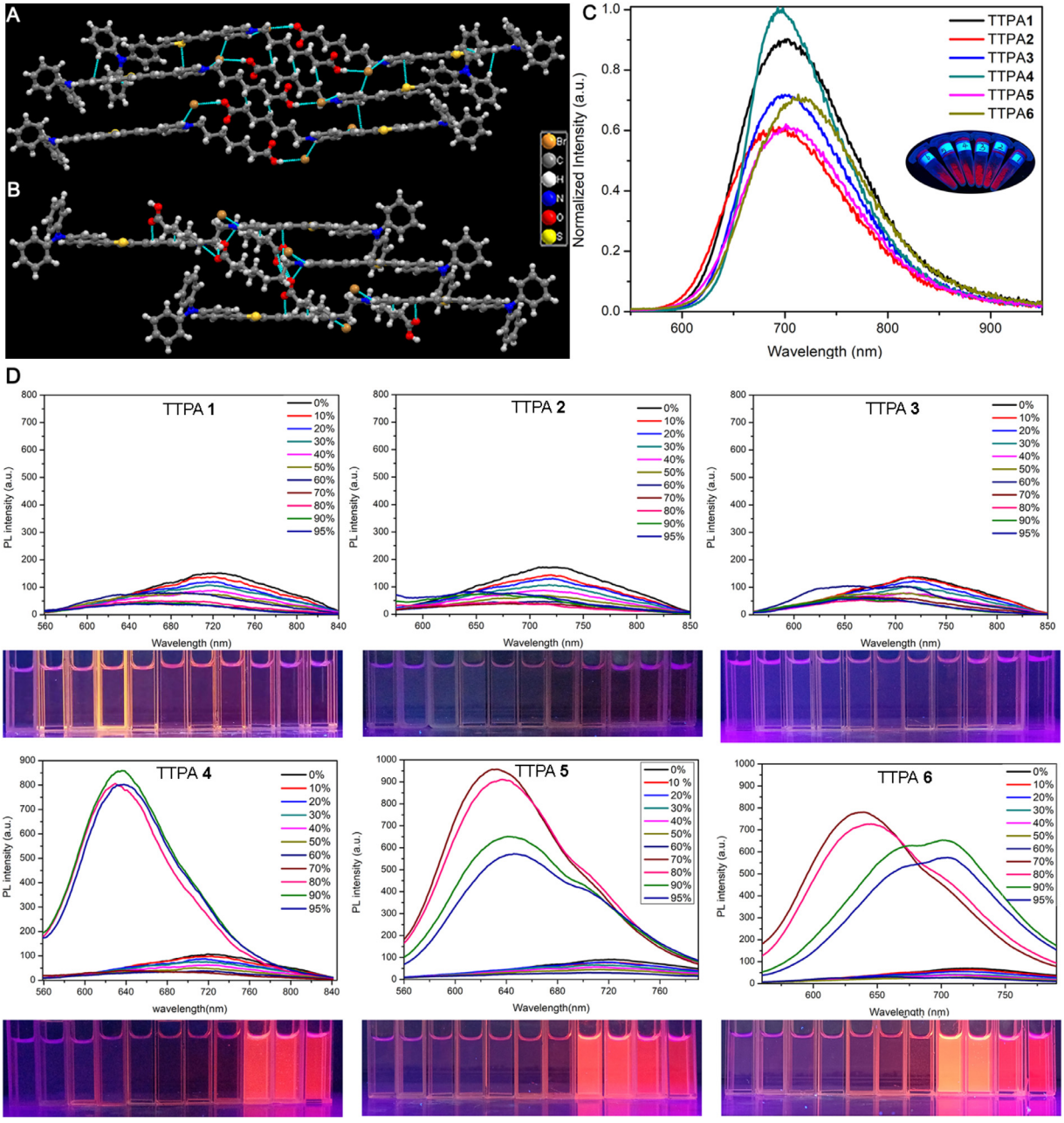

Fig. 1 – (A) and (B) The packing structure of the crystals of TTPA 3, TTPA 4 (the blue dotted lines indicate the intermolecular interactions); (C) Fluorescence spectra of solid powdered TTPAs 1–6 and (D) the fluorescent probe (1.00×10^{-5} mol/l) at different water content (λex = 498 nm) in menthol.

2.21. *PDT effect TTPA 4–6 nanoparticles in vivo*

As the volume of the tumor reached about 100 mm^3, the mice were intervened by intravenous injection with 200 μl PBS (-Light), PBS and TTPAs **4–6** at Day 0 and 2. Specifically, the dose of TTPA **4**, TTPA **5** and TTPA **6** were 20 (it tends to aggregation at high water content as shown in Fig. 1D), 40 and 40 μM, respectively. In addition, the 4T1 tumors of PBS, TTPA **4**, TTPA **5** and TTPA **6** groups were exposed to white light irradiation for 5 min (0.2 W/cm^2) at 4 h post-injection. Additionally, the body weight and tumor volume of each mouse were measured every other d. Finally, the mice were sacrificed on Day 13, and the tumors were collected and weighed. In order to evaluate the bio-safety of the TTPAs **4–6**, the major organs, including hearts, livers, lungs, spleen, and kidneys were collected and evaluated by the hematoxylin and eosin (H&E) staining and the apoptotic tumors tissues were evaluated by terminal deoxynucleotidyl transferase labeling (TUNEL).

2.22. *Statistical analysis*

All data were obtained from three independent trials. The statistical significance was determined using a one-way analysis of variance followed by Graphpad PRISM 6.02, and

the P value < 0.05 was considered as the minimal level of significance. [CCDC: 2225802, TTPA **3** and 2225803, TTPA **4** contains the supplementary crystallographic data that can be obtained from the Cambridge Crystallographic Data Centre via www.ccdc.cam.ac.uk/data_request/cif. for this paper.]

3. Results and discussion

3.1. *Design and synthesis*

Since strong fluorescence-emission of AIE fluorogens (AIEgens) persists in the aggregated state or high concentration, AIEgens show greater advantages than most ACQ dyes for use in cancer imaging. Therefore, a large number of drug delivery systems with AIE characteristics have been used for image-guided cancer therapy. In particular, molecules with donor-π-acceptor (D-π-A) structures have been demonstrated to have unique benefits to be photosensitizers for photodynamic cancer therapy or photothermal therapy. In this work, we have designed a series of AIE molecules bearing D-π-A structural features. In the synthesized TTPAs **1–6**, the TPA units serve as strong electron donors (D) and the pyridinium moiety acts as an electron acceptor (A), whilst the carboxyl group was introduced in order to improve the hydrophilic ratio. Furthermore, based on the alkyl chain length, the potential can be tuned, which in turn allows for the cellular uptake and localization to be controlled *via* different alkyl chain lengths for the TTPA molecules. Fortunately, X-ray quality red single crystals of TTPA **3** and TTPA **4** suitable for single crystal X-ray analysis were obtained by slow evaporation of a saturated ethanol solution. The key crystal data for TTPA **3** and TTPA **4** are summarized in Table S1; both TTPA **3** and TTPA **4** belong to the triclinic crystal system. As shown in Fig. 1, in the packing of the structure, the TTPA **3** molecules are connected by intermolecular π-π interactions (~3.36 Å) and multiple C–H···O hydrogen bonds between adjacent molecules. Furthermore, these intermolecular forces enable the TTPA **3** molecules to adopt a compact parallel arrangement, which results in the alkyl chains being in a staggered parallel arrangement and wrapped inwards (Fig. 1A); note the alkyl chain is disordered in TTPA **4**. In the molecular structure of TTPA **4**, molecules are connected by multiple C–H···O hydrogen bonds and C–H···π interactions between adjacent molecules, forming a loosely packed arrangement (Fig. 1B). As the alkyl chain length increases, the interaction between molecules decreases and the arrangement between molecules becomes more and more disordered. Thus, it is evident that the change in carbon chain length changes the configuration of the molecules in the aggregation state to a large extent, which impacts the optical properties of the molecules in terms of AIE.

Additionally, all the TTPAs **1–6** exhibit similar observed solid-luminescence as shown in Fig. 1C. Furthermore, the quantum yield (Φ) and the fluorescence lifetime (t) are given in Table S2. In addition, we also recorded the UV/vis spectra and fluorescence emission spectra of the TTPAs **1–6** in different solvents and found that they all exhibit similar results. Moreover, all the TTPA molecules exhibit the strongest fluorescence emission in $CHCl_3$ solvent (Fig. S13). Meanwhile, they have an absorption peak at 526 nm and a broad emission spectrum ranging from 570 nm to 850 nm (Fig. S14) in $CHCl_3$. Studies of the AIE characteristics in methanol/water mixtures with different water components (f_w) indicate (Fig. 1D) that it is almost non-emissive on increasing the percentage of water component present for TTPAs **1–3**. By contrast, TTPAs **4–6** exhibited a significant fluorescence intensity increase once the f_w exceeded 70 %, which revealed an obvious AIE property. This is mainly because the rotational motion of the molecular rotor consumes exciton energy and increases non-radiative decay rates, leading to non-emission. Due to the formation of aggregates, with the increase in water content and alkyl chain length, the hydrophobicity of the system was enhanced, and the photoluminescence (PL) intensity gradually increased.

3.2. *Light-triggered ROS generation of TTPAs 1–6 in solution*

DCFH, a general commercial indicator of ROS generation, was utilized to measure the total generated ROS by the TTPAs **1–6** irritated with white light (~50 mW/cm^2), given that the ROS play a role in PDT. Easy-to-obtain, non-toxic white light was utilized as the irradiation source to help the six TTPA molecules generate ROS. The results in Figs. 2A and S15 revealed that nearly all the AIEgens (TTPAs **1–6**) exhibited significant enhancement of fluorescence intensity compared with the equivalent concentration (10 μM) of free Ce6 upon exposure to white light irradiation (~50 mW/cm^2) over a fairly short irradiation time (within 60 s). Consequently, this result and other reported research data reveal that the highly efficient ROS generation of AIE photosensitizers is down to the smaller singlet and triplet energy gap caused by the stronger donor-acceptor effect, which is conducive to the intersystem crossing process from singlet state to triplet state and greatly improves the yield of the triplet excited state.

3.3. *Hydroxyl radical species generation of TTPAs 1–6 in solution*

For the hydroxyl radical species (·OH), known as type I ROS, the generation rate was further evaluated by use of the commercially available HPF. As expected, the fluorescence intensity of TTPAs **1–6** was dramatically elevated under white light irritation, whereas the ·OH generation in the free Ce6 group was barely visible (Figs. 2B and S16). Unlike type II ROS, ·OH can contribute to significant cytotoxicity through superoxide dismutase (SOD)-mediated disproportionation reaction. What's more, cascade bio-reactions triggered by ·OH can subsidize extra oxygen *in situ*, which further ameliorates the hypoxia environment at the tumor site and paves the way for PDT [45].

3.4. *Detection of $^1O_2$ generation of TTPAs 1–6 in solution*

The efficiency of the type II ROS of $^1O_2$ is conducive to PDT, and ABDA was used in this assay to evaluate $^1O_2$ generation. Furthermore, in order to evaluate the $^1O_2$ productivity accurately, the commonly utilized photosensitizer Ce6 was selected as a type II ROS reference. As shown in Figs. 2C and S17, the absorption peak of ABDA hardly changed when

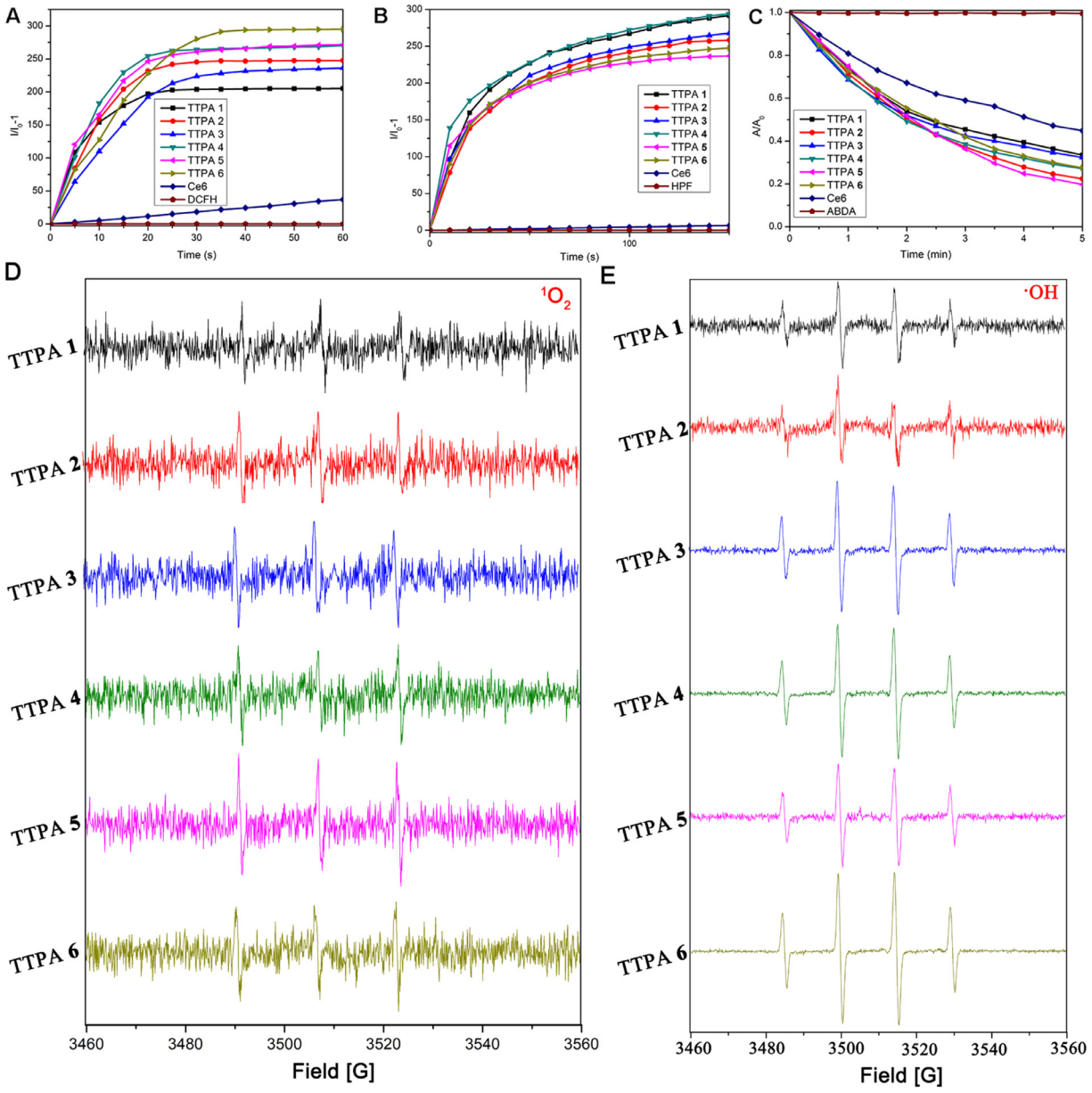

Fig. 2 – (A) Plots of relative PL intensity of DCFH (for total ROS measurement) and (B) HPF (for ·OH detection); (C) Plots of decomposition rates of ABDA (for $^1O_2$ determination) in the presence of TTPAs 1–6 or free Ce6 in PBS *versus* irradiation time; (D) ESR signals of TEMP (for $^1O_2$ determination) and (E) DMPO (for ·OH detection) in the presence of TTPAs 1–6 after irradiation.

subjected to irritation over differing time periods, while all six TTPAs demonstrated a significantly reduced absorption rate under equal light irradiation. Compared with the equivalent concentration of free Ce6, a most significant evident reduction in ABDA absorbance was observed for the TTPA **1–6** molecules. This shows that the TTPA molecules possess a higher $^1O_2$ production capacity than the widely used photosensitizer free Ce6 when using the same dosage.

3.5. *Detection of types of ROS by ESR analysis*

ESR technology is very important for the detection of ROS species. Therefore, the spin-trap agent of TEMP was used to survey the generation of type II ROS ($^1O_2$) and TEMP was used to survey the generation of type I ROS (·OH). Expectedly, all molecules have no signal when interacting with the trapping agent in dark (Fig. S18). However, all show the typical ESR signals of products formed by singlet oxygen free radicals and the trapping agent TEMP [46] after irradiated, as shown in Fig. 2D. Particularly, TTPAs **3–6** exhibited significantly stronger ESR signals, which implied better ability to produce the type I ROS (Fig. 2E) [40].

3.6. *Cellular uptake analysis of TTPAs 1–6*

We then measured the intracellular fluorescence intensity of TTPAs **1–6,** given that cellular uptake is an important parameter affecting a molecule's activity. As shown in

Fig. S19, these results are consistent with the particle size measurements above. It is worth noting that all of the six groups showed strong fluorescence intensity, and the ability of staining cells was positively correlated with the length of the alkyl chain. From this, we inferred that a suitable side chain can effectively improve the membrane permeability of a fluorescent probe and increase self-delivery. By comparison with the literature [30], the membrane permeability of probes bearing C6-C10 side-chains is more than 76-fold higher than that with a C1 side-chain. Meanwhile, the smallest particle size of TTPA **5** contributes to its strongest fluorescence intensity among the TTPA **4–6** molecules.

3.7. *3D tumor penetration of TTPAs 1–6*

The tumor sphere penetration of a drug can determine its tumor-killing effect [47]. To verify whether TTPAs **1–6** possess excellent tumor penetration ability *in vitro*, 3D tumor spheroids were established to simulate the tumor microenvironment. From Fig. 3A, with the increase of tumor depth, drug penetration decreased gradually. In particular, when the tumor depth was 100 μm, only faint fluorescence was detected at the edge of the tumor spheroids in the TTPA **3–6** group, while they were invisible in TTPAs **1** and **2**. Notably, the tumor spheroid carrying TTPA **5** demonstrated a strong TTPA fluorescence in the center of the tumor sphere at the depth of 80 μm, which revealed that the TTPA **5** possessed best tumor penetration among the three groups.

3.8. *Cellular distribution assay of TTPAs 1–6*

In order to observe the mitochondrial or lysosomal targeting effects of the TTPA **1–6** molecules, the mito-tracker and lyso-tracker were used to visualize these two organelles in green. Thereafter, with the entrance of the TTPAs **1–6** into lysosome and mitochondria, the red fluorescence emitted by the molecules merged with the green marker of the mitochondria or lysosomal, thus resulting in yellow. As shown in Fig. S20, scattered green and red dots were observed in the TTPA **1** and TTPA **2** groups at 0.5 h, especially the TTPA **1** group, whereas yellowish green pinpoints were clearly visible in the TTPA **3–6** groups, which exhibited stronger interaction rate of longer alkyl chain TTPA molecules. On extending the interaction time, the superposition of the fluorescence coming from the TTPAs **1–6** and from the lysosome was seen as a yellow color, suggesting that almost all the TTPAs **1–6** entered the lysosome of the cells. Furthermore, the Pearson correlation coefficient (PCC) values between the TTPA molecules and the lyso-tracker 2 h after the TTPA molecules were added into cells was calculated. From Fig. S21, it can be observed that all the PCC values between the TTPA molecules and lysosomes were around 0.9, which suggests all molecules are swallowed up by the cells via a caveolin-mediated endocytosis pathway. In addition, the overwhelming majority of TTPA **1–6** molecules swarm into the lysosomes and interact with H^+ to increase the positivity of the TTPAs **1-6**, and this provides the prerequisites for targeting the mitochondria. Therefore, we also tested the Zeta potential at pH 4.5, as shown in Fig. S22. Clearly, TTPAs **4–6** exhibit stronger positivity, which may be due to the fact that the longer the alkyl chain, the farther the carboxyl group is from the electron-drawing pyridine cation. In other words, the weaker acidity leads to a weakened dissociation ability of the carboxyl group, and so the surface positivity is stronger. From Fig. 3B, it can be seen that the PCC values between the Mito-tracker and TTPA **4**, TTPA **5** and TTPA **6** are determined to be 0.93, 0.97 and 0.98, respectively, which are conducive to the generation of ROS. Nevertheless, the PCC values for TTPA **1**, TTPA **2** and TTPA **3** were relatively small, especially that for TTPA **1**, which was only 0.63. The mitochondrial targeting effect of TTPAs **4–6** was much higher than that of TTPAs **1–3**. This is likely a result of their potential and longer alkyl chains enhancing the interaction with the mitochondrial membrane [32].

3.9. *Mitochondrial superoxide generation of TTPAs 1–6*

To further prove the mitochondria targeting of TTPAs **1–6**, Mito-SOX, a mitochondrion-targeting probe, which is sensitive to the production of mitochondrial superoxide, was employed [48]. The TTPA **4** to TTPA **6** groups displayed stronger superoxide generation ability than did TTPA **1** to TTPA **3** (Fig. 3C). This may be due to the length of the alkyl chain being proportional to the interaction with the mitochondrial membrane. Additionally, TTPA **5** is much stronger than the other groups.

3.10. *Intracellular ROS generation of TTPAs 1–6*

DCFH-DA reacts with intracellular ROS to produce detectable fluorescent substances, as a consequence, DCFH-DA was used to evaluate the ROS generated by cells that had been incubated with the TTPA **1–6** molecules and irradiated by white light. As shown in Fig. 4A, the PBS (-Light) and PBS groups were both dim, indicating negligible generated ROS. Among the light-irradiated groups, strong fluorescence and necroptosis were observed for the TTPA **1** to TTPA **6** groups, especially for the TTPA **5** group. The fluorescence intensity of TTPA **1** was a little weaker than that of TTPA 2 and TTPA 3, which may be attributed to the shortest membrane permeability. Additionally, the TTPA **4** to TTPA **6** groups revealed strong ROS generation which may be the result of their assembly ability with albumin. To verify these results, flow cytometry was used for a quantitative determination of the green fluorescence (Fig. 4B). When the cells were only exposed to white light (PBS), the percentage of green fluorescence demonstrated very limited change from 0.57 % (PBS group) to 0.79 %. As expected, the order of fluorescence percentage in all the TTPA molecules was TTPA **5**≈TTPA **6**>TTPA **4**, which further verified the results observed by CLSM.

3.11. *Mitochondrial morphology assays after treatment with TTPAs 1–6*

To investigate the effect of the TTPAs **1–6** photodynamic action on mediated PDT, we used transmission electron microscopy to observe changes in mitochondrial ultrastructure after PDT. As depicted in Fig. 4C, the mitochondria in the 4T1 cells in the PBS group possess distinct and complete membrane structures with a smooth outer membrane and intact inner membrane. However, all

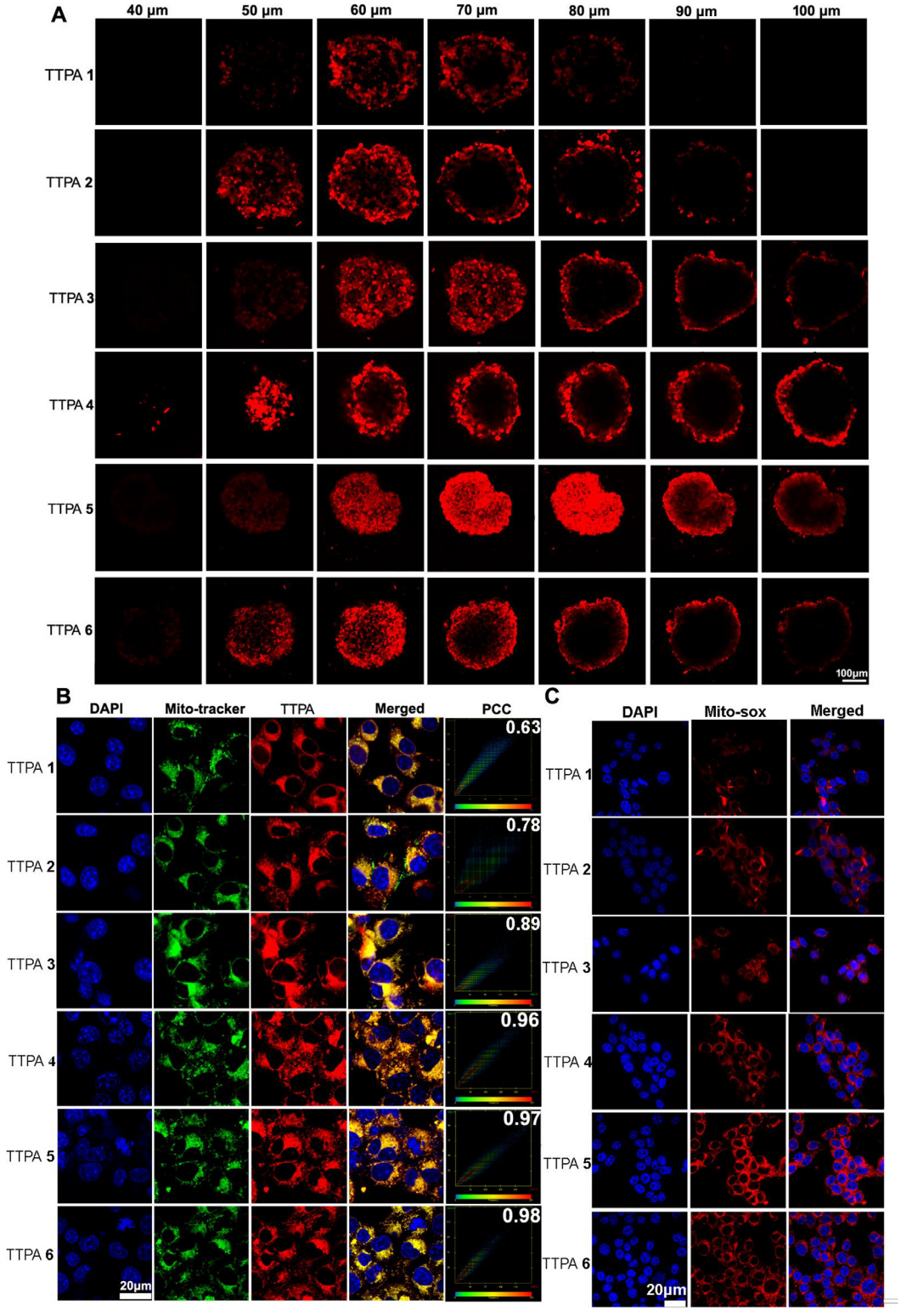

Fig. 3 – (A) Penetration ability of TTPAs 1–6 into 4T1 tumor spheroids (scale: 100 μm); (B) Confocal images of 4T1 cells treated with TTPAs 1–6 at 2 h, TTPA (red), mitochondria were stained with Mito-Tracker (scale: 20 μm); (C) Confocal images of mitochondrial superoxide generation by Mito-SOX staining in cells incubated with TTPAs 1–6, blue and red represent. (scale: 20 μm).

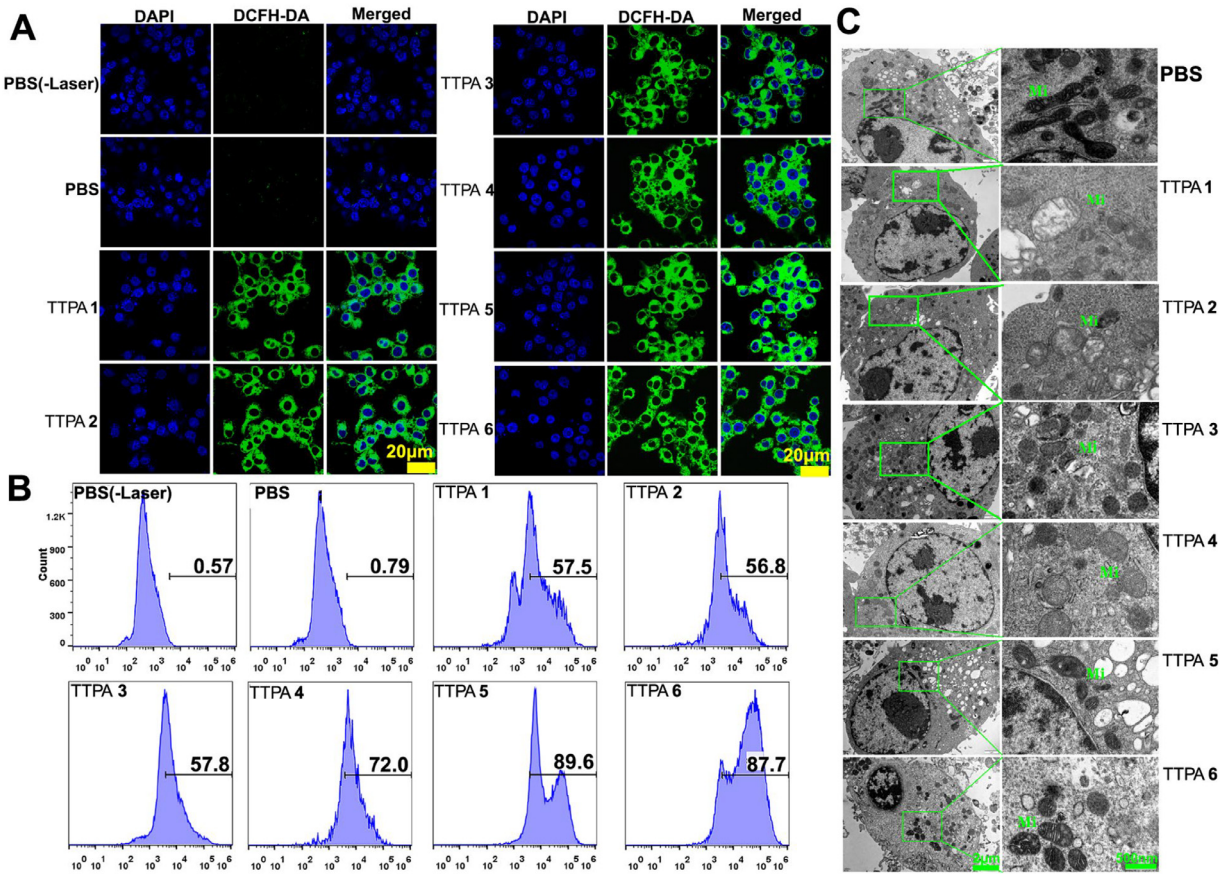

Fig. 4 – (A) and (B) Confocal images and flow cytometry results of ROS generation in 4T1 cells incubated with PBS (-Light), PBS, TTPA 1–6 (blue: DAPI; green: DCFH-DA; scale bar: 20 μm) to evaluate ROS generation by DCFH-DA; (C) Morphological changes of mitochondria observed by TEM.

the mitochondria in the TTPA groups displayed destruction to differing degrees. The structural images of the mitochondria unveiled distorted and swelling cristae, and the mitochondria swell into a circular shape. Additionally, in the TTPA **5** and TTPA **6** groups, the inner membrane of the mitochondria was entirely destroyed, and the whole of the mitochondria contracted. What's even worse for the 4T1 cells in these two groups is that there were a large number of voids present, and the amount of mitochondria was reduced in the cytoplasm. These results reveal that the TTPAs **1–6** directly give rise to rapid damage to the mitochondria morphology following PDT.

3.12. *PDT effect of TTPAs 1–6 in vitro*

The PDT effects of the TTPAs were estimated by Calcein AM/PI staining assays and a CCK8 test. The Calcein AM/PI staining results (Fig. 5A) revealed that almost all of the 4T1 cells in the TTPA **1–6** groups were colored by the PI, indicating that almost all cells were killed. Simultaneously, the pictures in Fig. 5B–D indicated that the proliferation inhibition rate of almost all cells was higher than 90 % when the TTPA dose was above 50 μM. Furthermore, TTPA **4** to TTPA **6** showed the highest cell proliferation inhibition efficiency, and even at relatively low concentrations (3.125 and 6.25 μM), the cell viability rate was still <20 %. Among the three tumor cells (B16F10, CT26, and 4T1) that were tested, the 4T1 cells showed the maximum mortality rate.

3.13. *Dark toxicity assay of TTPAs 1–6*

The CCK8 assays were applied to evaluate the dark toxicity of TTPAs **1–6** without light-irradiation, and the results are presented in Fig. 5E. The PBS (-Light) and PBS groups exhibited near-complete green fluorescence, which indicated no phototoxicity. In contrast to the phototoxicity results shown in Fig. 5B–D, there was no significant cytotoxicity for the 4T1 cells treated with TTPAs **1–6** even at a concentration of 25 μM without light irradiation, whereas almost all cells died under light irradiation at the same concentration. As a consequence, the high tumor cell-killing efficacy of TTPAs **1–6** is attributed to the generation of large amounts of ROS.

3.14. *Self-assembly and formation of TTPAs 4–6 with albumin*

Based on the better photodynamic effect of TTPAs **4–6** in the cell experiments, we further studied the state of the TTPAs **4–**

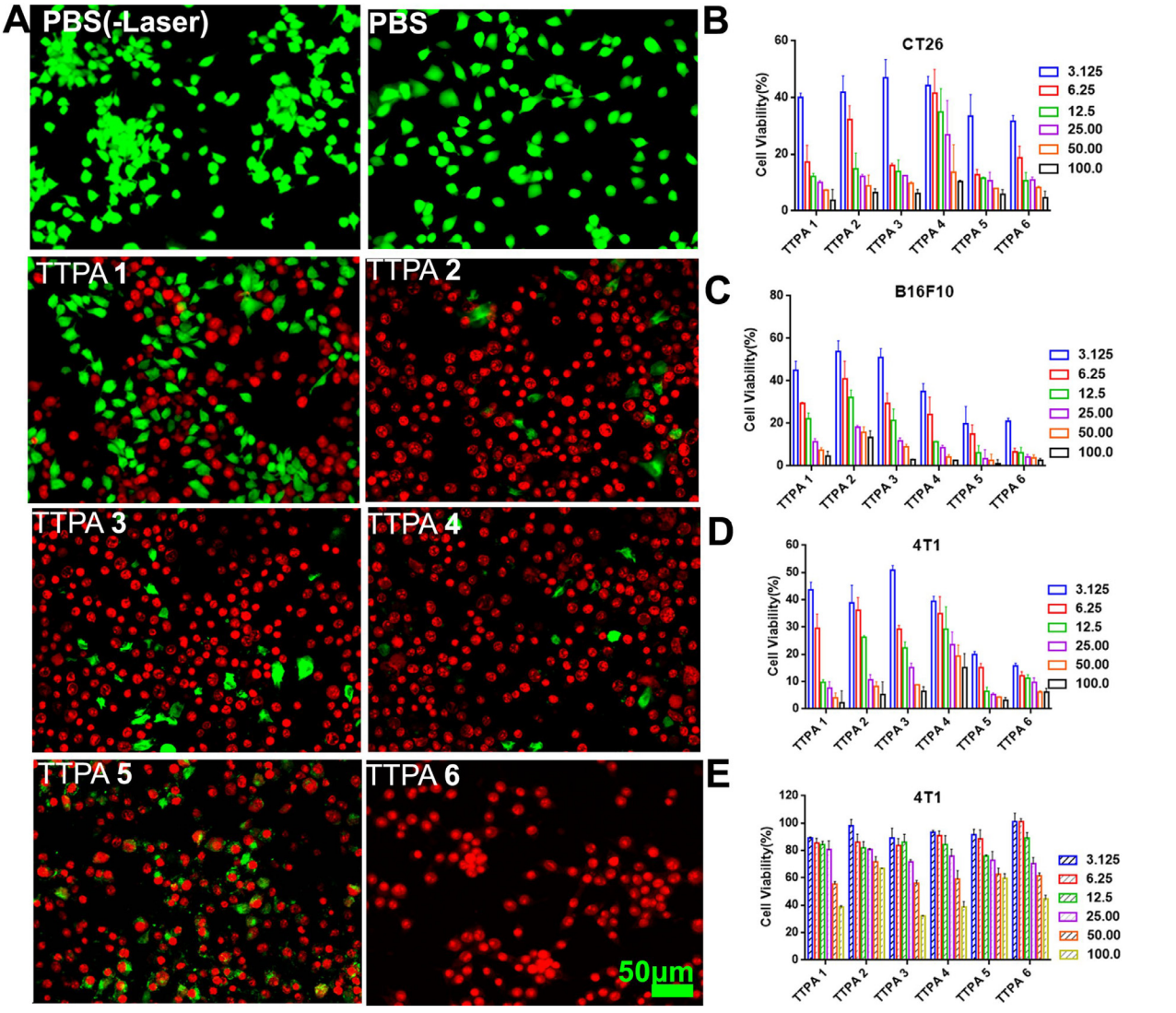

Fig. 5 – (A) Fluorescence images of Calcein AM/PI stained cells treated with TTPAs 1–6 and irradiated with white light (5 min, 50 mW/cm^2) (scale bar: 50 μm); (B-D) Phototoxicity of TTPAs 1–6 with white light irradiation (5 min, 50 mW/cm^2) on CT26, B16F10 and 4T1 cells; (E) Relative cell viabilities after incubation with various concentrations of TTPAs 1–6 for 48 h (dark-toxicity).

6 present in the extracellular fluid environment. Considering the large amount of albumin present in the plasma, the interaction of TTPAs **4–6** and albumin was investigated. The results demonstrated that TTPAs **4–6** could form a colloidal solution and the DLS size of TTPAs **4–6** are presented in Fig. 6A–C, which reveals that the TTPAs **4–6** can assemble with albumin to form TTPA **4–6** based nanoparticles (*i.e.*, TTPA **4**-NPs, TTPA **5**-NPs, TTPA **6**-NPs). In addition, a large number of bromide ions exist in the TTPAs **4–6**, which results in negatively charged molecules. Simultaneously, the morphology of the TTPA **4–6** nanoparticles was studied by TEM. The data in Fig. 6D–F illustrates that the TTPA **4–6** nanoparticles are homogeneous spheroids with particle sizes <200 nm, and that the TTPA **5**-NPs exhibited the smallest size (124.11 ± 7.8 nm) and greatest Tyndall effect. It is clear that albumin is abundant in the complete culture medium and blood serum. Thus, the results herein provide sufficient evidence for the further application of TTPA **4–6** nanoparticles *in vivo*.

3.15. *Fluorescence intensity measurements of the assembling of TTPAs 4–6 with albumin*

In order to investigate whether the assembly of TTPAs **4–6** and albumin can positively influence the aggregation-induced emission effect of the TTPA **4–6** molecules, the fluorescence intensity of TTPAs **4–6**, with or without albumin present, was measured using a spectrofluorometer. The results are shown in Fig. 6E–G and reveal that the fluorescence intensity of the TTPAs **4–6** is dramatically enhanced when assembled with albumin, which paves the way for effective PDT of tumors *in vitro* and *in vivo*.

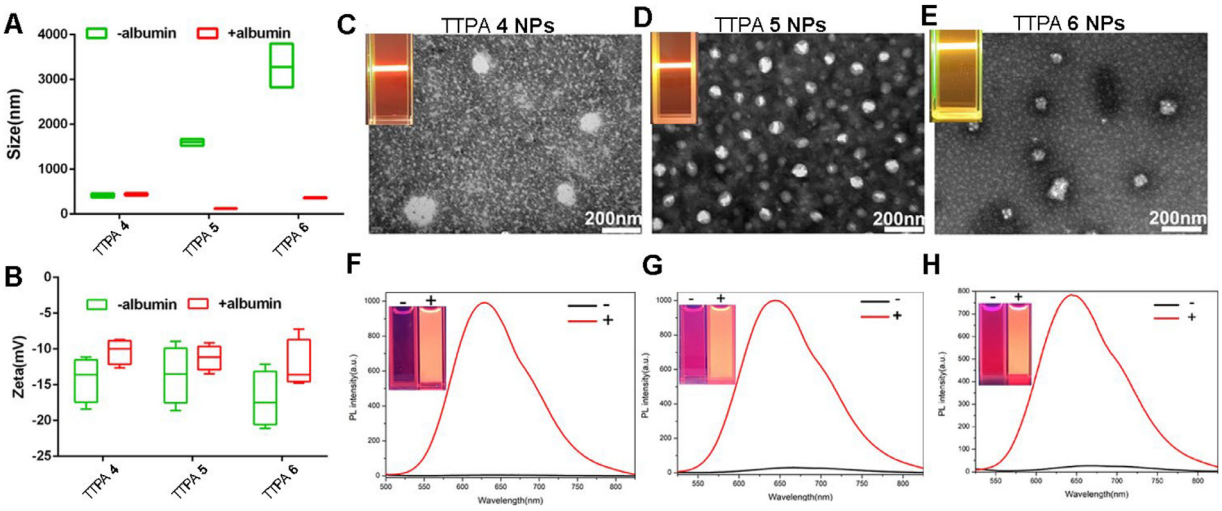

Fig. 6 – (A) and (B) size distribution and zeta potential of TTPAs 4–6 and TTPA 4–6 NPs; (C-E) Morphology of TTPA 4–6 NPs; (F-H) Fluorescence spectra of TTPAs 4–6 without and with the presence of albumin (-albumin or +albumin), the TTPA 4–6 NPs were prepared from TTPAs 4–6 (10 μM, in PBS with 1 % DMSO) and the final concentration of albumin was 10 μM.

3.16. *Molecular docking simulation of the assembling of TTPAs 4–6 with albumin*

Molecular docking simulations were performed to investigate in more detail how the TTPA molecules bind to albumin. As shown in Fig. 7, the carboxyl group is located at the surface of the molecule in the domain. However, the triphenylamine is close to the hydrophobic binding pocket in the domain, which results in the albumin wrapping around the whole TTPA molecule [49]. For TTPA **4**, the residue of Tyr 137 and Phe 133 can form hydrogen bonds with the carboxyl group, and the strengths of the hydrogen bonds are 3.04 Å and 2.47 Å, respectively (Fig. 7A and Table S3). Furthermore, there are multiple C–H···π interactions between phenyl and thienyl groups involving residues of Tyr137, Tyr160, Arg144, Pro420 and Leu462. Additionally, TTPA **5** and TTPA **6** show similar interactions with albumin as does TTPA **4**, whereas TTPA **5** binds more closely to the residue of Tyr 137 (2.87 Å), Phe 133 (1.98 Å) and Tyr160 (2.33 Å) (Fig. 7A and C and Table S3) and forms stronger multi-hydrogen bonds in comparison to TTPA **4** and TTPA **6**. Consequently, TTPA **5** shows the strongest interaction with albumin, which is thought to be the reason for the smallest particle size of the TTPA **5** NPs.

3.17. *pH response of TTPAs 4–6 assembled with albumin*

Given that the weak acidic microenvironment (pH 6.5–6.8) of the tumor tissue is lower than that of normal tissue (~pH 7.4), we also investigated the PL intensity changes of TTPA+albumin under pH 2–12 conditions (Fig. S23). Three aggregation-induced emission nano-photosensitizers (TTPA+albumin) were then obtained by mixing each of TTPAs **4–6** with albumin, respectively. At a pH below 7, TTPA+albumin exhibits weak PL intensity, which is conducive to *in vivo* application. However, when the pH is greater than 7, the fluorescence intensity was clearly enhanced, which is likely due to the TTPA reassembling with the albumin. Given that free TTPA molecules in DMSO are almost non-emissive under pH 2–12 (Fig. S23), it demonstrates that TTPA+albumin is pH-responsive and that the assembly is broken down when the pH is below 7.

3.18. *In situ assembly of TTPA 4–6 nanoparticles in blood*

As shown in Fig. 8A–C, all of TTPAs **4–6** exhibit strong red emissions in plasma and blood around 640 nm, similar to the trend observed in Fig. 6E–G. Therefore, this result clearly shows that the assembly of TTPAs **4–6** with albumin can be quickly and stably generated *in situ* in blood.

3.19. *In vivo tumor targeting effect of TTPA 4–6 nanoparticles*

Moreover, the *in vivo* distributions of the three assembled TTPA molecules (TTPAs **4–6**) were detected by a 4T1 tumor-bearing mouse model. Consequently, as shown in Fig. 8D, whole-body fluorescence was observed in the three groups at 0.25 h post-injection from blood circulation. As time progressed, the nanoparticles assembled with the albumin and the TTPA **4**, TTPA **5** or TTPA **6** molecules were enriched in the tumor sites due to angiogenesis. Especially at 4 h post-injection, the NIR emission intensity at the tumor sites was strong in the TTPA **5** and TTPA **6** groups, which provides a basis for the irradiation time of PDT *in vivo*. Moreover, among the three groups, the TTPA **5** treated mice presented the strongest tumor accumulation among the three groups, and exhibited tumor sites that remain even after 24 h. The semi-quantitative data based on the *in vivo* imaging of the tumor site groups indicated the order of fluorescence intensity in the three groups was TTPA **5**>TTPA **6**>TTPA **4**, probably due to the smallest particle size of TTPA **5** (Fig. 8E).

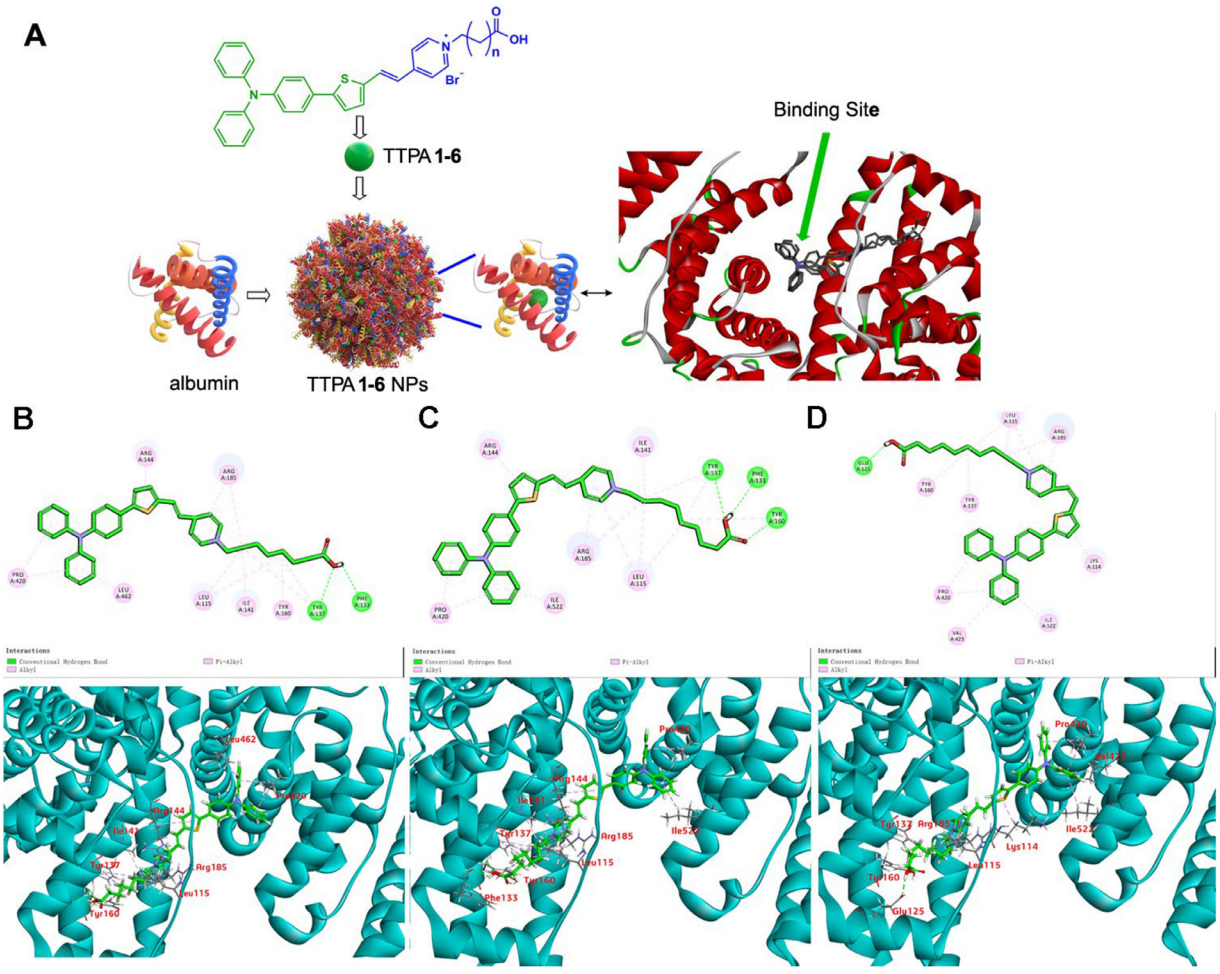

Fig. 7 – (A) Schematic illustration of the TTPA 4–6 NPs construction; (B-D) The binding mode and hydrogen bonds formed between albumin and TTPAs 4–6, respectively.

3.20. *In vivo PDT efficacy of TTPA 4–6 nanoparticles*

The *in vitro* PDT results suggested that TTPA **4**, TTPA **5**, and TTPA **6** exert enhanced cytotoxicity to 4T1 cells due to their assembly capacity. In addition, *in vivo* fluorescence targeting experiments showed that TTPA **4**, TTPA **5** and TTPA **6** could aggregate at the tumor site 4 h after injection, indicating that the concentration of PSs at the tumor site was high at this time, so it could visually guide the optimal time point of white light irradiation in PDT. Thus, in this experiment, the TTPA **4**, TTPA **5**, TTPA **6** and PBS were intravenously injected at Day 0 and 2 and white light exposed at 4 h post injection on the basis of the *in vivo* tumor targeting results. As shown in Fig. 8F-H, the tumor volume in the PBS (-Light) and PBS groups showed rapid and continuous growth, which indicated that the tumor-killing effect of the white light was almost negligible. By contrast, the TTPA molecule groups (including TTPA **4**, TTPA **5** and TTPA **6**) all possessed an extraordinary tumor inhibition effect, especially in the TTPA **5** group. This can be attributed to the smallest nanoparticle size formed by the self-assembly of the TTPA **5** molecules. In addition, from the tumor weight results, the cytotoxicity of the TTPA **5** molecules can almost be ignored.

Furthermore, for the purpose of investigating the tumor therapeutic efficacy of each TTPA molecule and their safety evaluation, an H&E staining and TUNEL assay were performed. The results are presented in Fig. S24. The H&E staining results revealed that the main organs in all groups showed a regular cell morphology with no abnormal inflammatory cell infiltration in each group after treatment. However, the H&E staining pictures of the tumor tissue in TTPA **4**, TTPA **5**, and TTPA **6** showed the nucleus pyknosis and the cytoplasm condensed, consistent with the tumor cells been seriously disrupted. Besides, the TUNEL expression unveiled that the apoptosis rate of the tumor cells in the TTPA **4**, TTPA **5**, and TTPA **6** groups was significantly higher than those in the PBS (-Light) and PBS groups (Fig. 8I). In short, these results show that the TTPA **4**, TTPA **5**, TTPA **6** molecules are effective at killing tumor cells *in vivo* to inhibit tumor growth.

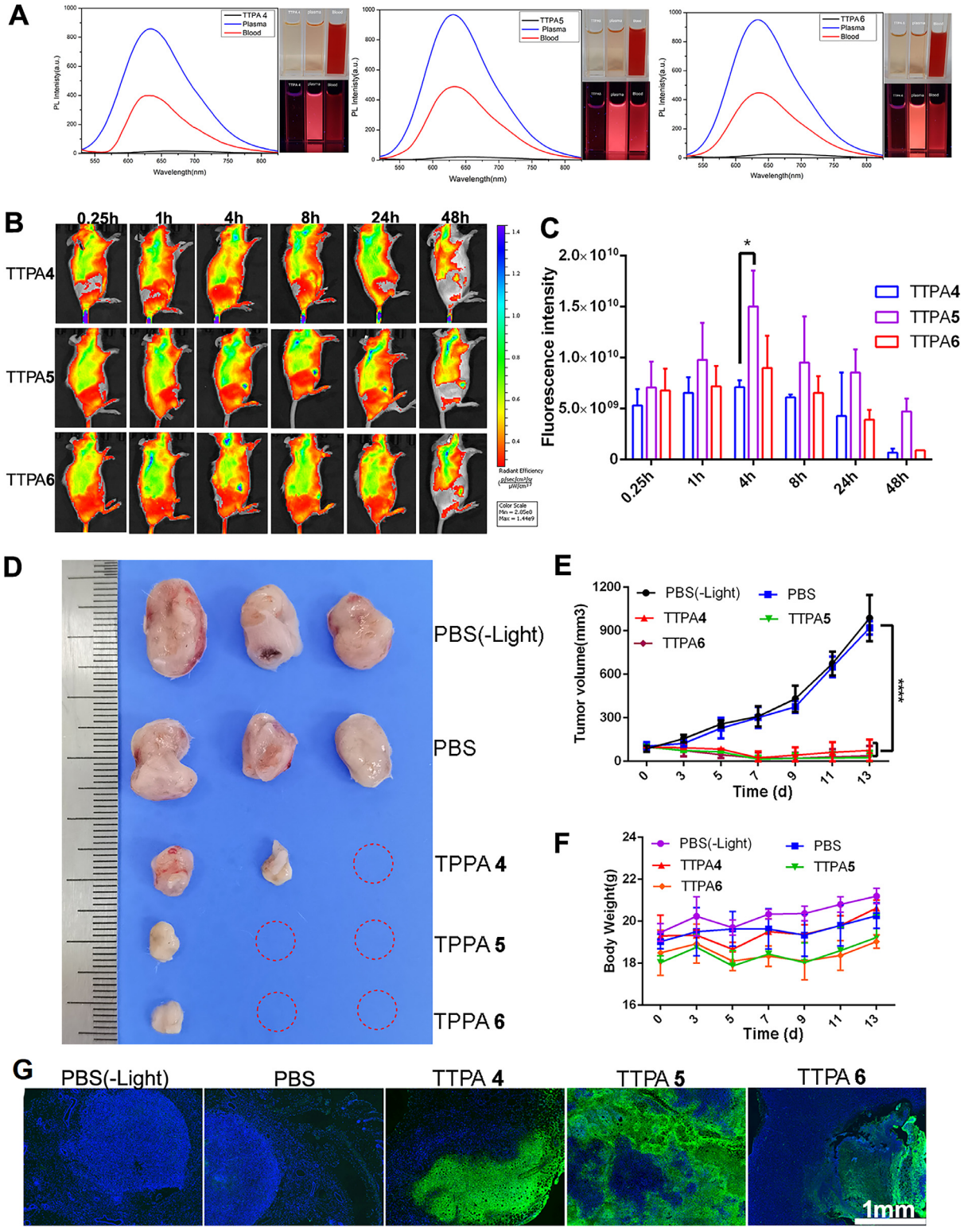

Fig. 8 – (A-C) TTPAs 4–6 formation of albumin complexes in blood; (D) Fluorescence images of 4T1 tumor-bearing mice after intravenous injection of different formulations; (E) Bar graph showing the semi-quantitative intensity of TTPAs 4–6 fluorescence signals, *P < 0.05; (F) Tumors collected from mice in different groups at Day 13; (G) Tumor volume in 4T1 tumor-bearing mice treated with different formulations (**P < 0.00001); (H) Body weight of mice bearing 4T1 tumors after various treatments; (I) Histological analysis of tumor slices after TUNEL assay (scale: 500 μm).**

4. Conclusion

In summary, we have synthesized six AIEgens named TTPAs **1–6**, which exhibited strong fluorescence in the aggregated state and were able to generate type I (·OH) and type II ($^1O_2$) ROS. They can be utilized for PDT under both aerobic and anaerobic conditions after rapidly been endocytosed by the cancer cells. In particular, the membrane permeability and targeting of TTPAs **4–6** bearing C8-C10 side-chains are higher than TTPAs **1–3** bearing shorter alkyl chains, which demonstrated that a simple chemical modification can dramatically improve the efficiency of PDT. Furthermore, the results of molecular docking, DLS and TEM unveiled that TTPAs **4–6** can assembled with albumin to form TTPA **4–6** NPs. The assembled TTPA **4–6** NPs can be targeted for delivery to intracellular mitochondria and further produce a large variety of ROS, even more efficiently than Ce6, resulting in extensive tumor cell damage. Beyond that, TTPAs **4–6** can assemble with albumin simultaneously after intravenous injection into the blood vessel, then the assembled TTPAs **4–6** can enrich the tumor sites owing to their pH responsiveness and nano-size effect. Finally, *in vivo* phototherapy with breast tumor-bearing mice shed light on the fact that AIE structural features endorse TTPAs **4–6** with NIR fluorescence for imaging and excellent PDT effect for tumor cell killing. Consequently, this work reveals that the TTPA molecules can yield an outstanding PDT effect and are ideal candidates for NIR imaging-guided tumor therapy.

Conflicts of interest

The authors report no conflicts of interest. The authors alone are responsible for the content and writing of this article.

Acknowledgments

This work was supported by the National Natural Science Foundation of China (81860543, 32360237), Guizhou Provincial Science and Technology Projects (ZK[2023] Key Project 041, ZK[2021]076, [2019]2792 and [2018]5779-14) and Guizhou Provincial Department of Education Foundation (KY[2022]229), Cultivation program of the Affiliated Hospital of Guizhou Medical University (gyfynsfc-2022-39), Cultivation program of the Guizhou Medical University (20NSP012). CR thanks the University of Hull for support.

Supplementary materials

Supplementary material associated with this article can be found, in the online version, at doi:10.1016/j.ajps.2024.100967. The figures and tables with "S" before the serial number are included in the Supplementary material.

References

[1] Sung H, Ferlay J, Siegel RL, Laversanne M, Soerjomataram I, Bray F. Global cancer statistics 2020: GLOBOCAN estimates of incidence and mortality worldwide for 36 cancers in 185 countries. CA Cancer J Clin 2021;71:209–49.
[2] Wang C, Guan J, Chen B, Xu L, Chen C. Progress of breast cancer basic research in China. Int J Biol Sci 2021;17:2069–79.
[3] Song K, Song J, Lin K, Chen F, Ma X, Li F. Survival analysis of patients with metastatic osteosarcoma: a surveillance, epidemiology, and end results population-based study. Int Orthop 2019;43:1983–91.
[4] Liu M, Chen Y, Guo Y, Yuan H, Cui T, Yao S, et al. Golgi apparatus-targeted aggregation-induced emission luminogens for effective cancer photodynamic therapy. Nat Commun 2022;13:2179.
[5] Zhou M, Liu X, Chen F, Yang L, Yuan M, Fu D, et al. Stimuli-activatable nanomaterials for phototherapy of cancer. Biomed Mater 2021;16:042008.
[6] Kim E, Park S, Kim YK, Moon M, Park J, Lee KJ, et al. Self-luminescent photodynamic therapy using breast cancer targeted proteins. Sci Adv 2022;6:eaba3009.
[7] Yang C, Fu Y, Huang C, Hu D, Zhou K, Hao Y, et al. Chlorin e6 and CRISPR-Cas9 dual-loading system with deep penetration for a synergistic tumoral photodynamic- immunotherapy. Biomaterials 2020;255:120194.
[8] Luo Q, Sun W, Li Z, Sun J, Xiao Y, Zhang J, Zhu C, Liu B, Ding J. Biomaterials-mediated targeted therapeutics of myocardial ischemia-reperfusion injury. Biomaterials 2023;303:122368.
[9] Li X, Chen L, Huang M, Zeng S, Zheng J, Peng S, et al. Innovative strategies for photodynamic therapy against hypoxic tumor. Asian J Pharm Sci 2023;18:100775.
[10] Kwiatkowski S, Knap B, Przystupski D, Saczko J, Kędzierska E, Kulbacka J. Photodynamic therapy-mechanisms, photosensitizers and combinations. Biomed Pharmacother 2018;106:1098–107.
[11] Wan Y, Fu L, Li C, Lin J, Huang P. Conquering the hypoxia limitation for photodynamic therapy. Adv Mater 2021;33:e2103978.
[12] Feng L, Li C, Liu L, Wang Z, Chen Z, Yu J, et al. Acceptor planarization and donor rotation: a facile strategy for realizing synergistic cancer phototherapy via type I PDT and PTT. ACS Nano 2022;16:4162–74.
[13] Yu Y, Wu S, Zhang L, Xu S, Dai C, Gan S, et al. Cationization to boost both type I and type II ROS generation for photodynamic therapy. Biomaterials 2022;28:121255.
[14] Chen M, Yang J, Zhou L, Hu X, Wang C, Chai K, et al. Dual-responsive and ROS-augmented nanoplatform for chemo/photodynamic/chemodynamic combination therapy of triple negative breast cancer. ACS Appl Mater Interfaces 2022;14:57–68.
[15] Yang C, Su M, Luo P, Liu Y, Yang F, Li C. A photosensitive polymeric carrier with a renewable singlet oxygen reservoir regulated by two NIR beams for enhanced antitumor phototherapy. Small 2021;17:e2101180.
[16] Huang Y, Lai H, Jiang J, Xu X, Zeng Z, Cui S, et al. pH-activatable oxidative stress amplifying dissolving microneedles for combined chemo-photodynamic therapy of melanoma. Asian J Pharm Sci 2022;17:679–96.
[17] Xu J, Lai Y, Wang F, Zou Z, Pei R, Xu Z, et al. Dual stimuli-activatable versatile nanoplatform for photodynamic therapy and chemotherapy of triple-negative breast cancer. Chin Chem Lett 2019;15:311–18.
[18] Wang S, Rong M, Li H, Xu T, Bu Y, Chen L, et al. Unveiling mechanism of organic photogenerator for hydroxyl radicals generation by molecular modulation. Small 2022;18:e2104857.
[19] Ni J, Min T, Li Y, Zha M, Zhang P, Ho CL, et al. Planar AIE gens with enhanced solid-state luminescence and ROS generation for multidrug-resistant bacteria treatment. Angew Chem Int Ed Engl 2020;59:10179–85.

[20] Zhao H, Li N, Ma C, Wei Z, Zeng Q, Tang B, et al. An AIE probe for long-term plasma membrane imaging and membrane-targeted photodynamic therapy. Chinese Chem Lett 2023;34:107699.
[21] Liu P, Gao C, Chen H, Vong CT, Wu X, Tang X, et al. Receptor-mediated targeted drug delivery systems for treatment of inflammatory bowel disease: opportunities and emerging strategies. Acta Pharm Sin B 2021;11:2798–818.
[22] Wang H, Zhao E, Lam JWY, Tang B. AIE luminogens: emission brightened by aggregation. Mater Today 2015;28:365–77.
[23] Zhang W, Kwok RT, Chen Y, Chen S, Zhao E, Yu C, et al. Real-time monitoring of the mitophagy process by a photostable fluorescent mitochondrion-specific bioprobe with AIE characteristics. Chem Commun (Camb) 2015;51:9022–5.
[24] Liu J, Liu X, Wu M, Qi G, Liu B. Engineering living mitochondria with AIE photosensitizer for synergistic cancer cell ablation. Nano Lett 2020;20:7438–45.
[25] Huang Y, You X, Wang L, Zhang G, Gui S, Jin Y, et al. Pyridinium-substituted tetraphenylethylenes functionalized with alkyl chains as autophagy modulators for cancer therapy. Angew Chem Int Ed Engl 2020;59:10042–51.
[26] Wen H, Zhang Z, Kang M, Li H, Xu W, Guo H, et al. One-for-all phototheranostics: single component AIE dots as multi-modality theranostic agent for fluorescence-photoacoustic imaging-guided synergistic cancer therapy. Biomaterials 2021;274:120892.
[27] Wu W, Shi L, Duan Y, Xu S, Shen L, Zhu T, et al. Nanobody modified high-performance AIE photosensitizer nanoparticles for precise photodynamic oral cancer therapy of patient-derived tumor xenograft. Biomaterials 2021;274:120870.
[28] Li Y, Wu Q, Kang M, Song N, Wang D, Tang Z. Boosting the photodynamic therapy efficiency by using stimuli-responsive and AIE-featured nanoparticles. Biomaterials 2020;232:119749.
[29] Cheng G, Wang H, Zhang C, Hao Y, Wang T, Zhang Y, et al. Multifunctional nano-photosensitizer: a carrier-free aggregation-induced emission nanoparticle with efficient photosensitization and pH-responsibility - ScienceDirect. Chem Eng J 2020;390:12447.
[30] Bashford CL, Smith JC. The use of optical probes to monitor membrane potential. Methods Enzymol 1979;55:569–86.
[31] Guo L, Li C, Shang H, Zhang R, Li X, Lu Q, et al. A side-chain engineering strategy for constructing fluorescent dyes with direct and ultrafast self-delivery to living cells. Chem Sci 2020;11:661–70.
[32] Rodriguez ME, Azizuddin K, Zhang P, Chiu SM, Lam M, Kenney ME, et al. Targeting of mitochondria by 10-N-alkyl acridine orange analogues: role of alkyl chain length in determining cellular uptake and localization. Mitochondrion 2008;8:237–46.
[33] Zhu H, Fan J, Du J, Peng X. Fluorescent probes for sensing and imaging within specific cellular organelles. Acc Chem Res 2016;49:2115–26.
[34] Zhang R, Niu G, Li X, Guo L, Zhang H, Yang R, et al. Reaction-free and MMP-independent fluorescent probes for long-term mitochondria visualization and tracking. Chem Sci 2019;10:1994–2000.
[35] Sheybani N, Yang H. Pediatric ocular nanomedicines: challenges and opportunities. Chin Chem Lett 2017;28:1817–21.
[36] Li A, Zhao J, Fu J, Jia C, Zhang P. Recent advances of biomimetic nano-systems in the diagnosis and treatment of tumor. Asian J Pharm Sci 2021;16:161–74.
[37] Zhou J, Chizhik AI, Chu S, Jin D. Single-particle spectroscopy for functional nanomaterials. Nature 2020;579:41–50.
[38] Krieg R, Eitner A, Gunther W, Halbhuber KJ. Optimization of heterocyclic 4- hydroxystyryl derivatives for histological localization of endogenous and immunobound peroxidase activity. Biotech Histochem 2007;82:235–62.
[39] Li Y, Ren T, Dong W. Tuning photophysical properties of triphenylamine and aromatic cyano conjugate-based wavelength-shifting compounds by manipulating intramolecular charge transfer strength. J Photochem Photobiol A 2013;251:1–9.
[40] Zhao X, Dai Y, Ma F, Misal S, Qi Z. Molecular engineering to accelerate cancer cell discrimination and boost AIE-active type I photosensitizer for photodynamic therapy under hypoxia. Chem Eng J 2020;410:128133.
[41] Hu D, Zhong L, Wang M, Li H, Qu Y, Liu Q, et al. Perfluorocarbon-loaded and redox-activatable photosensitizing agent with oxygen supply for enhancement of fluorescence/photoacoustic imaging guided tumor photodynamic therapy. Adv Funct Mater 2019;29:1806199.
[42] Yuan X, Nie W, He Z, Yang J, Shao B, Ma X, et al. Carbon black nanoparticles induce cell necrosis through lysosomal membrane permeabilization and cause subsequent inflammatory response. Theranostics 2020;10:4589–605.
[43] Chen Q, Li Q, Liang Y, Zu M, Chen N, Canup BSB, et al. Natural exosome-like nanovesicles from edible tea flowers suppress metastatic breast cancer via ROS generation and microbiota modulation. Acta Pharm Sin B 2022;12:907–23.
[44] Zeng L, Xia T, Hu W, Chen S, Chi S, Lei Y, et al. Visualizing the regulation of hydroxyl radical level by superoxide dismutase via a specific molecular probe. Anal Chem 2018;90:1317–24.
[45] Ehrenberg B, Montana V, Wei MD, Wuskell JP, Loew LM. Membrane potential can be determined in individual cells from the nernstian distribution of cationic dyes. Biophys J 1988;53:785–94.
[46] Zheng L, Zhu Y, Sun Y, Xia S, Duan S, Yu B, et al. Flexible modulation of cellular activities with cationic photosensitizers: insights of alkyl chain length on reactive oxygen species antimicrobial mechanisms. Adv Mater 2023;35:2302943.
[47] Haycock JW. 3D cell culture: a review of current approaches and techniques. Methods Mol Biol 2011;695:1–15.
[48] Kwon HJ, Cha M, Kim D, Kim DK, Soh M, Shin K, et al. Mitochondria-targeting ceria nanoparticles as antioxidants for Alzheimer's disease. ACS Nano 2016;10:2860–70.
[49] Tayeh N, Rungassamy T, Albani JR. Fluorescence spectral resolution of tryptophan residues in bovine and human serum albumins. J Pharm Biomed Anal 2009;50:107–16.